Article

Cell Reports

How Does the *Xenopus laevis* Embryonic Cell Cycle Avoid Spatial Chaos?

Graphical Abstract

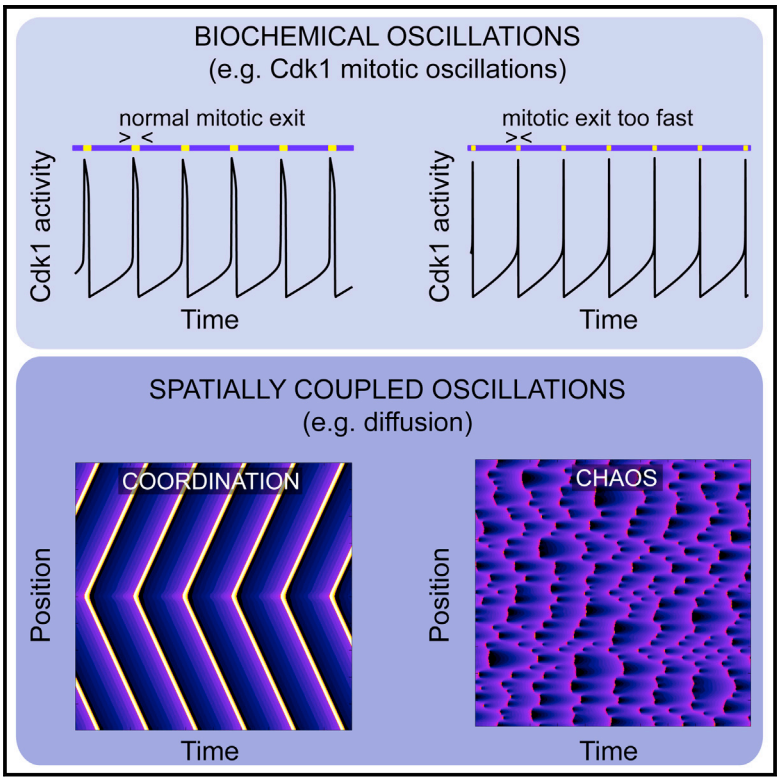

Authors

Lendert Gelens, Kerwyn Casey Huang, James E. Ferrell, Jr.

Correspondence

lendert.gelens@gmail.com

In Brief

Recent studies have suggested that the *Xenopus* embryonic cell cycle could be susceptible to chaotic arrhythmias. Here Gelens et al. show that the cell cycle operates reliably in the face of perturbations predicted to cause chaos and examine how chaos can be generated or avoided in spatially coupled relaxation oscillators.

Highlights

- Spatially coupled relaxation oscillators of short pulse duration can generate chaos
- Spatial heterogeneities can trigger a transition to chaotic dynamics
- Mitotic exit in the *Xenopus laevis* cell cycle is likely slow enough to avoid chaos
- Spatial chaos can be a feature or a hazard in biology

Gelens et al., 2015, Cell Reports *12*, 1–9
August 4, 2015
http://dx.doi.org/10.1016/j.celrep.2015.06.070

CellPress

Please cite this article in press as: Gelens et al., How Does the *Xenopus laevis* Embryonic Cell Cycle Avoid Spatial Chaos?, Cell Reports (2015), http://dx.doi.org/10.1016/j.celrep.2015.06.070

Cell Reports
Article

How Does the *Xenopus laevis* Embryonic Cell Cycle Avoid Spatial Chaos?

Lendert Gelens,[1,2,*] Kerwyn Casey Huang,[3,4] and James E. Ferrell, Jr.[1,5]
[1]Department of Chemical and Systems Biology, Stanford University School of Medicine, Stanford, CA 94305-5174, USA
[2]Applied Physics Research Group, Vrije Universiteit Brussel (VUB), 1050 Brussels, Belgium
[3]Department of Bioengineering, Stanford University, Stanford, CA 94305-5444, USA
[4]Department of Microbiology and Immunology, Stanford University School of Medicine, Stanford, CA 94305-5124, USA
[5]Department of Biochemistry, Stanford University School of Medicine, Stanford, CA 94305-5307, USA
*Correspondence: lendert.gelens@gmail.com
http://dx.doi.org/10.1016/j.celrep.2015.06.070

SUMMARY

Theoretical studies have shown that a deterministic biochemical oscillator can become chaotic when operating over a sufficiently large volume and have suggested that the *Xenopus laevis* cell cycle oscillator operates close to such a chaotic regime. To experimentally test this hypothesis, we decreased the speed of the post-fertilization calcium wave, which had been predicted to generate chaos. However, cell divisions were found to develop normally, and eggs developed into normal tadpoles. Motivated by these experiments, we carried out modeling studies to understand the prerequisites for the predicted spatial chaos. We showed that this type of spatial chaos requires oscillatory reaction dynamics with short pulse duration and postulated that the mitotic exit in *Xenopus laevis* is likely slow enough to avoid chaos. In systems with shorter pulses, chaos may be an important hazard, as in cardiac arrhythmias, or a useful feature, as in the pigmentation of certain mollusk shells.

INTRODUCTION

In the amphibian *Xenopus laevis*, embryogenesis begins when the sperm penetrates the cell-cycle-arrested egg, initiating a wave of elevated cytoplasmic calcium that brings about the completion of meiosis II and allows the mitotic cell cycles to begin (Gerhart, 1980; Hausen and Riebesell, 1991). The first mitotic cleavage occurs approximately 85 min after fertilization and is followed by 11 rapid, 25-min cell cycles that lead up to the mid-blastula transition. These rapid early embryonic cell cycles are remarkably regular, with the cell cycle period varying little from cycle to cycle and from cell to cell.

These cell cycle oscillations are driven by a biochemical oscillator circuit centered on the cyclin B-cyclin-dependent kinase 1 (Cdk1) complex (Minshull et al., 1989; Murray and Kirschner, 1989). The oscillator circuit possesses a bistable trigger (Goldbeter, 1993; Novak and Tyson, 1993b; Pomerening et al., 2003; Sha et al., 2003), which is built from interlinked positive (Cdk1 activates Cdc25, which activates Cdk1) (Hoffmann et al., 1993; Solomon et al., 1990) and double-negative (Cdk1 inhibits Wee1 and Myt1, which inhibit Cdk1) (McGowan and Russell, 1993; Mueller et al., 1995a, 1995b; Parker and Piwnica-Worms, 1992; Tang et al., 1993) feedback loops. As levels of cyclin B rise during S phase, the switch eventually flips, driving the cell irreversibly into mitosis. Mitotic exit is then initiated through a negative feedback loop involving the anaphase-promoting complex/cyclosome (APC/C^{Cdc20}), which polyubiquitinates cyclin B, tagging it for degradation by the proteosome (Cdk1 activates APC/C^{Cdc20}, which inhibits Cdk1) (King et al., 1996). The strengths and response functions of the different feedback loops have been experimentally measured using *Xenopus* extracts (Kim and Ferrell, 2007; Pomerening et al., 2003, 2005; Trunnell et al., 2011; Tsai et al., 2014; Yang and Ferrell, 2013), providing a detailed quantitative accounting of the biochemical reactions of the cell cycle oscillator.

Much can be learned by considering a biochemical oscillator circuit to be a system of spatially uncoupled homogeneous biochemical reactions that can be modeled by ordinary differential equations (ODEs). This assumption is well justified for very small or well-stirred systems. However, the *Xenopus* egg is neither. This underscores the need to examine the spatial dynamics of cell cycle oscillations as well as the temporal dynamics. The first model to include spatial diffusion of all proteins involved in the early cell cycle control system was recently presented by McIsaac et al. (2011). Surprisingly, the authors noticed that the system had the potential to generate spatially chaotic dynamics. Although it is well known that ODE cell cycle models can generate temporal chaotic oscillations (Romond et al., 1999), in this case the reactions of the ODE model were not chaotic, and chaos emerged only once diffusive spatial coupling was added to the model. In particular, the authors used simulations to predict that if the post-fertilization calcium wave were slowed down even by a factor of two compared to its physiological speed, chaotic cell cycle oscillations would emerge, giving rise to an unpredictable patchwork of cell divisions across the embryo.

Using the same biochemical model as in McIsaac et al. (2011), Figure 1 illustrates these two different types of spatial dynamics in a periodic system of diffusively coupled cell cycle oscillators. This model (see Experimental Procedures) was numerically

Please cite this article in press as: Gelens et al., How Does the *Xenopus laevis* Embryonic Cell Cycle Avoid Spatial Chaos?, Cell Reports (2015), http://dx.doi.org/10.1016/j.celrep.2015.06.070

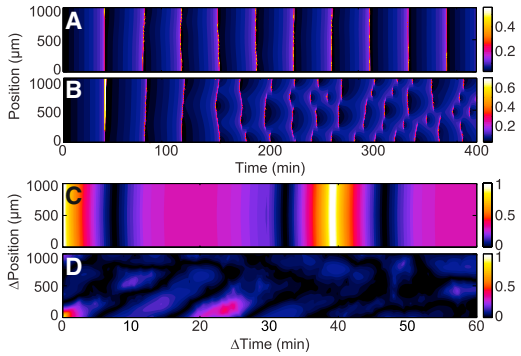

Figure 1. A Slower Calcium Wave Leads to Chaotic Dynamics in a Cell Cycle Model

(A and B) Simulated time series of Cdk1 activity using cell cycle model 1 (see Supplemental Information) where the cell cycle oscillations are initiated upon passing of (A) a fast calcium wave, with speed *vel* = 50 μm/s, and (B) a slow wave, with *vel* = 10 μm/s. Shown is the activity of Cdk1 as a function of position and time, in arbitrary units.

(C and D) Spatio-temporal correlations. (C) Correlation for (A). (D) Correlation for (B). Periodic boundary conditions were assumed; only half of the domain is shown.

evaluated in a system with periodic boundary conditions. The kinetic parameters were taken to be uniform over the whole space, but the oscillations were initiated at different times at different positions as determined by when the calcium wave passed that location. This leads to spatial heterogeneity in the initiation time of cell cycle oscillations.

For a fast calcium wave, the oscillations are nearly synchronous (Figure 1A). However, when the calcium wave is slowed down, synchrony is lost. Instead, different regions in space exhibit transient oscillatory dynamics with constantly evolving periods and amplitudes (Figure 1B). This loss of synchrony is confirmed by the spatio-temporal correlation function (Figures 1C and 1D). For a fast calcium wave, there is strong correlation over all space at zero time difference and at time differences corresponding to integer multiples of the period of the cell cycle oscillations (Figure 1C). For the slowed calcium wave, such correlations no longer exist, although correlation signatures can still be found, mainly around half of the cell cycle period (Figure 1D). Thus, it appears that this shift from spatially synchronized to complex, poorly coordinated spatial dynamics represents a transition into chaos. In this work, we will use the term chaos to describe any irregular dynamics that are poorly correlated in space and time, that have a deterministic chaotic attractor (see Figure 4), and that have different responses with respect to slight changes in initial conditions (see Figure S1).

Intrigued that chaos might be lurking so close to the normal physiological operating range of the cell cycle oscillator, we set out to test this hypothesis experimentally. In this study, we demonstrate that cell divisions proceed with their normal near synchrony even when the calcium wave is slowed down by a factor of ~2. We then investigated why the in vivo system displays less tendency for chaos than the model system. We found that the model becomes most susceptible to transitions into chaos when the cell cycle oscillations have a very short pulse duration of Cdk1 activation, probably shorter than in the physiological case (Pomerening et al., 2003; Tsai et al., 2014; Yang and Ferrell, 2013). Finally, to see whether there is a general link between the pulse duration of the oscillatory reactions and the propensity of a spatially distributed system to exhibit chaos, we made use of the FitzHugh-Nagumo model, a well-explored model in physics and theoretical biology inspired by the action potential. In general, it appears that any heterogeneity, be it a slow calcium wave or a heterogeneous distribution of biochemical parameters in space, can trigger a chaotic response if coupled with oscillatory reactions with sufficiently short pulses. Thus, the observed spatial dynamics put constraints on the temporal dynamics of the biochemical reactions.

RESULTS

Xenopus Embryos with Slow Calcium Waves Show No Evidence of Chaotic Cell Division

We hypothesized that one way to slow the initial calcium wave would be to transiently cool the fertilized egg. To this end, we designed a setup that allows precise and accurate control of the temperature of eggs and embryos. This setup consists of a chamber with a capacity of several hundred embryos (Figure 2A). The temperature of the aluminum chamber is electrically controlled to ±0.01°C using Peltier elements. We fertilized eggs in this device at various temperatures and measured the velocity of the calcium wave by monitoring the pigment rippling that accompanies the wave. As has been previously noted, the calcium wave propagated approximately linearly from the sperm entry point to the opposite side of the embryo (Busa and Nuccitelli, 1985; Fontanilla and Nuccitelli, 1998). Therefore, we could estimate the speed of the calcium wave by constructing kymographs and fitting a straight line to the observed wave of pigment changes (Figure 2B; Movies S1 and S2). The calcium wave speed increased approximately linearly with temperature, ranging from 4.5 μm/s at 13°C to about 9.3 μm/s at 23°C (Figure 2C). Thus, by decreasing the temperature from 23°C to 13°C, the calcium wave was slowed down by a factor of ~2.

We next compared subsequent cell cycle progression in embryos that were fertilized at 13°C and then returned to 23°C after the calcium wave had passed with embryos fertilized and maintained at 23°C. Data from one control 23°C/23°C and one 13°C/23°C embryo are shown in Figures 2D and 2E. The embryo fertilized in the cold underwent its mitotic divisions about 14 min after the control embryos. However, the embryonic cell cycles proceeded with a normal period, and there was no evidence of desynchronization across the embryo (Figures 2D and 2E; Movie S3). Moreover, both the control and 13°C/23°C embryos developed into healthy tadpoles (Figure 2E; Movie S3). Thus, there was no evidence for chaos in embryos whose cell cycles have been initiated by a slow calcium wave. The results shown in Figures 2D and 2E and Movie S3 are representative of the ~20 control and ~10 experimental embryos examined in each of eight independent experiments.

Spatially Coupling Relaxation Oscillators of Short Pulse Duration Leads to Chaos

This experimental finding prompted the question of why slower calcium waves do not seem to affect the correct development

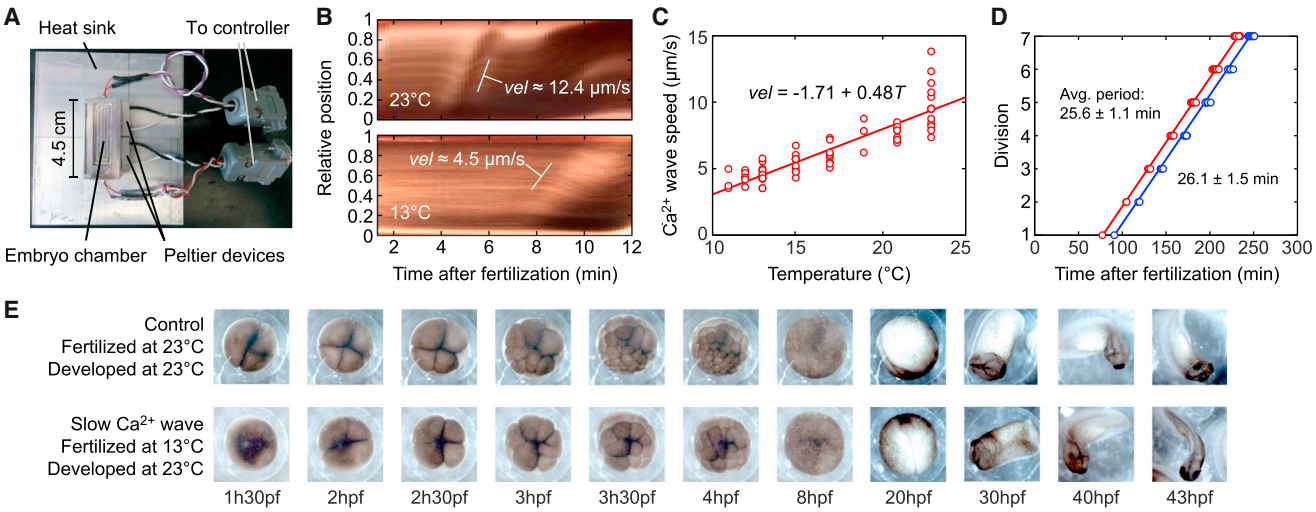

Figure 2. Slowing the Calcium Wave by Lowering Temperature Does Not Affect Synchronization or Embryonic Development

(A) Device to control the temperature of eggs and embryos.

(B) Kymographs showing the calcium wave after fertilization at T = 23°C and T = 13°C. Image contrast and brightness have been adjusted to accentuate the calcium waves. Wave speeds were estimated assuming that each embryo is 1.2 mm in diameter.

(C) The calcium wave speed increases with increasing temperature, as shown by data pooled from 12 independent experiments.

(D) The timing of cell division in one embryo fertilized at 13°C and then returned to 23°C after the calcium wave had passed (blue) and one embryo fertilized and maintained at 23°C (red). Each data point represents the division of one cell within the embryos. Note that as embryogenesis proceeds, cell division becomes metachronous, with cell division sweeping from one side of the embryo to the other. The pattern and timing of this metachronous cell division wave were indistinguishable in the control versus experimental embryos. Average periods are expressed as means ± SD.

(E) Video frames of the embryos analyzed in (D) at different time points, labeled by hours post-fertilization (hpf) (see also Movie S3).

of the *Xenopus* embryo. To address this question, we examined the underlying dynamical principles that are of importance in generating the chaotic waves observed in previous modeling studies (McIsaac et al., 2011). The model used in McIsaac et al. (2011) (and before that in Pomerening et al., 2003, 2005, hereafter referred to as cell cycle model 1; see Supplemental Information) consists of nine ODEs, including the various different phosphorylation states of the cyclin-B-Cdk1 complex and polo-like kinase 1 (Plx1) activity (Figure 3A). In a model with this high degree of complexity, it is relatively difficult to understand exactly why the spatial chaos emerged. More recently, a simpler (but still realistic) cell cycle model for the early *Xenopus* embryo was proposed containing only two ODEs, where the various parameters have been empirically determined (Yang and Ferrell, 2013) (Figure 3B; hereafter referred to as cell cycle model 2; see Supplemental Information). Using the latter model, no sign of chaos was observed, not even when dramatically slowing down the calcium wave (Figure 3H, top).

Why did one model produce chaos and the other did not? Comparison of the two models showed that in cell cycle model 1 the relaxation oscillations had a very short pulse duration (Figure 3D, bottom) (McIsaac et al., 2011), whereas in cell cycle model 2 they were longer (Yang and Ferrell, 2013), with a much slower time constant for the switch from high to low cyclin-B-Cdk1 levels (Figure 3E, top). To ascertain whether the profiles of these oscillations (short versus longer pulse duration) were important determinants of the generation of chaotic dynamics, we first decreased the rate of degradation due to APC/C by a factor of 100 in cell cycle model 1. This change prolonged the time spent in M phase and indeed restored the synchrony of mitosis (Figures 3D and 3G). Conversely, we increased the degradation rate due to APC/C by a factor of 10 in cell cycle model 2, which decreased the pulse duration of the oscillation reactions (Figure 3E) and triggered chaotic dynamics (Figure 3H). Finally, we also verified these results in a third cell cycle model introduced by Novak and Tyson (1993a). The cell cycle oscillations in this model had a more sustained M phase and therefore maintained their synchrony when diffusively coupled.

Although this observation suggested that chaotic dynamics might be generally triggered by spatially coupling short pulsatile relaxation oscillators in the presence of a slow calcium wave, it remained possible that this is a phenomenon specific to these particular cell cycle models. To address this, we examined a more generic model that admits relaxation oscillations, the FitzHugh-Nagumo (FHN) model (Fitzhugh, 1961; Nagumo et al., 1964), and added a parameter γ to alter the pulse duration of the oscillations (following the lead of Hall and Glass, 1999); see Supplemental Information). We found oscillations of long pulse duration for $\gamma = 0.01$ and oscillations with short pulses for $\gamma = 1$ (Figure 3F). Introducing spatial diffusive coupling into the FHN model produced the same transition from synchronous oscillations to chaotic dynamics as seen in the cell cycle models (Figures 3F and 3I), suggesting that the transition to chaos mediated by short pulses is a general phenomenon.

Dynamics in the FHN model can be interpreted in the two-dimensional phase space spanned by two variables: u, the rapidly changing variable, and v, the slowly changing variable. We examined the structure of the different long-term attractors

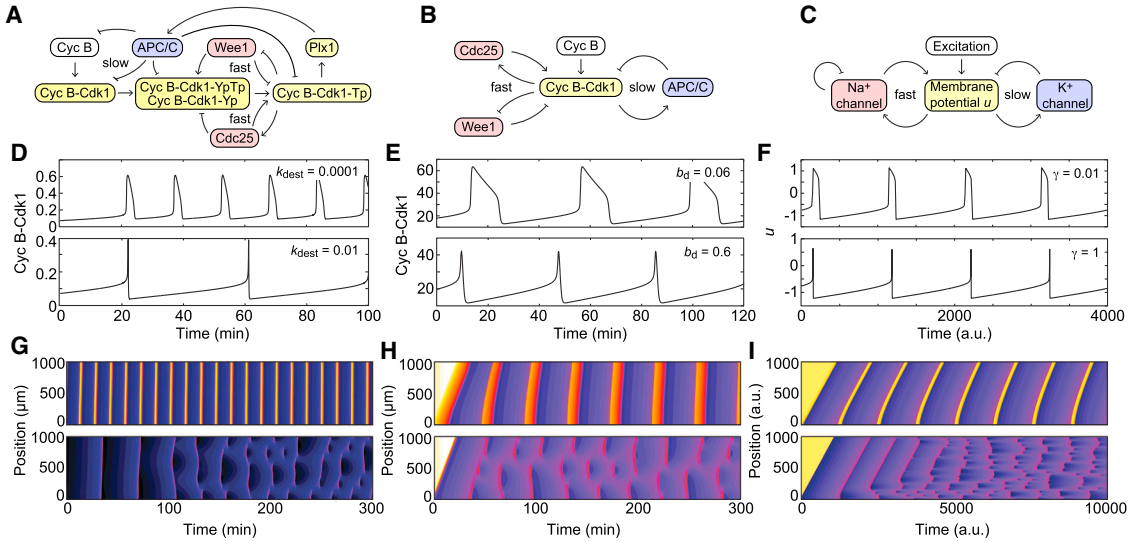

Figure 3. Duration of the Reaction Response Dictates the Transition to Chaotic Dynamics in Three Different Relaxation-Oscillator Models

(A–F) Cell cycle models. (A) Cell cycle model 1. (B) Cell cycle model 2. (C) The FHN model. In each case, changing one parameter resulted in a transition from long (top) to short (bottom) pulses, as shown in (D), (E), and (F) for the models in (A), (B), and (C), respectively.

(G–I) Spatial dynamics. (G) Spatial dynamics corresponding to (D), (H) spatial dynamics corresponding to (E), and (I) spatial dynamics corresponding to (F) as a result of introducing diffusive coupling. Oscillations were initiated after the passing of a calcium wave with speed *vel* = 10 μm/s in (G), *vel* = 10 μm/min in (H), and *vel* = 1 arbitrary unit in (I).

that exist in the FHN model and how those attractors are altered upon changes in the pulse duration of the oscillation reactions. We found that the FHN system can relax into two different attracting states depending on the reaction parameters of the system. First, the system can show a complex series of oscillations that are uncorrelated at points sufficiently separated in space and time (Figure 4A). The phase space plot in this case shows that the system does not have a simple periodic structure (Figure 4C). This is typical for a chaotic attractor and argues that the observed dynamics are in fact chaotic. Nonetheless, this chaotic attractor still has clear structure, whereby the trajectories visit the cubic Z-shaped nullcline deterministically and head toward the bottom leg at random times. Second, the system can instead relax into perfect synchronous oscillations when the pulses are longer, jumping back and forth between the two legs of the *u* nullcline (Figures 4B and 4D).

Spatial Heterogeneities Can Generally Trigger a Transition to Chaotic Dynamics

These findings argue that chaotic dynamics can generally arise when spatially coupled relaxation oscillators of short pulse duration are initiated at different times (Figures 3 and 4). Using the FHN model, we now turn to the question of whether other spatial heterogeneities can trigger a transition from synchrony to chaos. We explored three different ways of introducing a heterogeneous spatial distribution, either in the initial conditions (Figure 5A) or in the reaction parameters (Figures 5B and 5C).

First, we considered a system in which all reaction parameters are homogeneous in space, but the oscillations are initiated at times that vary linearly with their distance from a fixed point, corresponding to a spreading calcium wave. As above (Figures 3F and 3I), for small values of γ (long pulses) the waves remained correlated and slowly became more synchronous in time (Figure 5D). In contrast, for large values of γ (short pulses) the waves quickly broke up, lost correlation, and evolved chaotically (Figure 5G).

As a comparison, we next considered a system in which oscillations were initiated at the same time everywhere in space, and the heterogeneity was induced by varying the reaction parameter ε, which defines the slow timescale of the variable *v* and, as such, also controls the period of the oscillations. A small region at the center was assigned a slightly larger value of ε (Figure 5B) such that this region oscillates faster than its surroundings when spatially uncoupled. Upon inclusion of spatial diffusive coupling, for oscillations with longer pulses, a trigger wave originated from this central region and spread out with a fixed velocity until it controlled the entire space (Figure 5E). Trigger waves initiated in this fashion by pacemakers appear to be a common phenomenon in biology (Gelens et al., 2014). In the context of the cell cycle, trigger waves have been recently observed in cell-free *Xenopus* egg extracts. It has been suggested that the centrosome serves as a pacemaker that controls mitotic entry and exit in the early *Xenopus* embryo (Chang and Ferrell, 2013; Gelens et al., 2014), perhaps by concentrating pro-mitotic factors such as Cdc25 and cyclin B (Bonnet et al., 2008; Jackman et al., 2003).

At higher values of γ (short pulse duration), chaotic dynamics spread out with a constant speed in much the same manner as the trigger wave observed for oscillations with longer pulses (Figure 5H). These results suggest that perhaps any type of heterogeneity is able to trigger chaotic oscillations. To test this idea further, we varied one of the parameters in the FHN model, ε,

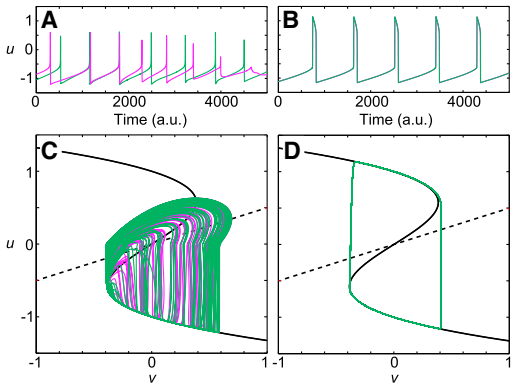

Figure 4. Both Chaotic and Periodic Dynamics Show a Clear Attractor in Phase Space

(A and B) Time series illustrating the long-term behavior of u in the spatially coupled FHN model with $\gamma = 1$ (A) and $\gamma = 0.01$ (B) at two locations: $x = 0$ (magenta) and $x = 250$ (green).

(C and D) Trajectories plotted in phase space, beginning after a transient of 15,000 time units. (C) Trajectory for the system shown in (A). (D) Trajectory for the system shown in (B). The u nullcline is shown in solid black, and the v nullcline in dashed black.

in a Gaussian noisy way (Figure 5C). For large values of γ (short pulses), the system indeed quickly developed chaos over the whole region (Figure 5I). In contrast, for small values of γ (long pulses), the spatially coupled oscillations emitted trigger waves that self-organized until eventually one location dominated the whole space (Figure 5F), closely resembling the mitotic waves observed in *Xenopus* egg extracts (Chang and Ferrell, 2013; Gelens et al., 2014). Diffusive processes that mix their immediate neighborhood are likely to orchestrate this self-organization process. Diffusion increasingly mixes large spatial regions as time increases according to the diffusion length given by $2\sqrt{Dt}$. In these simulations, the diffusion constant was $D = 1$, such that over a time interval of $t = 1{,}000$, ~60 length units become mixed. We applied a low-pass filter to the parameter distribution of ε, using a cut-off frequency based on this diffusion length (Figure 5C, dark blue). Strikingly, the locations of the primary local minima of this filtered response corresponded precisely to the points of origin of the trigger waves, and the global minimum ended up being the location of the dominant trigger wave (Figure 5F).

Thus, various types of heterogeneities can trigger chaos in the FHN system, provided that the reactions have a sufficiently short pulse duration. Such heterogeneities can arise in the initial conditions as demonstrated in McIsaac et al. (2011) or in reaction parameter values as shown here. We note that the influence of heterogeneities has been studied before in FHN systems, especially in the context of cardiac electrophysiology (Bub et al., 2002; Ermentrout and Rinzel, 1996; Panfilov et al., 2005; Prat and Li, 2003; Sridhar et al., 2010; Steinberg et al., 2006). However, in these works, the influence of pulse duration in the presence of heterogeneities had not been studied, which we show to be crucial to trigger a transition into chaos. Given how much biological heterogeneity would be expected in, for example, the *Xenopus* egg, it seems likely that the pulsatile oscillatory reactions are simply not short enough to support chaos. In other words, our measurement of spatial synchrony in the face of heterogeneities provides us with key information about the shape of the underlying local reaction processes, which are difficult to directly assess experimentally. It helps to explain the biological need to maintain M phase active for a sufficient amount of time. Various labs have noticed the presence of a time delay in the activation of the APC/C complex that starts mitotic exit by degrading cyclins (Vinod et al., 2013; Yang and Ferrell, 2013). Such a time delay can help to ensure a sufficient time in M phase to avoid spatial chaos.

Characteristics of the Transition into Chaos

Given that the pulse duration of the reactions plays an essential role in the generation of chaos, we asked whether diffusion strength could also promote or inhibit chaotic dynamics. Using the same central pacemaker region as in Figures 5E and 5H, we explored the dynamics for varying values of the pulse duration (γ) and the diffusion strength (D). We found that, at constant γ, decreasing the diffusion strength promoted the generation of chaotic dynamics (Figures 6A–6C). When D is decreased, the pacemaker in the center of the region loses its ability to dominate the whole space (Figure 6B). Such traveling wave instabilities have been widely studied in the context of cardiac and neural dynamics, where how they can be blocked and reflected (also referred to as back-propagation or echo waves) has been analyzed (Booth and Erneux, 1995; Deng, 1991; Ermentrout and Rinzel, 1996; Keldermann et al., 2007; Li, 2003; Rabinovitch et al., 1999; Zhou and Bell, 1994). In the current work, however, the region captured by the initial trigger wave shrinks as D decreases, multiple defects appear that eventually no longer vary periodically with time, and chaos sets in (Figure 6C). As shown in Figure 6D, there is a trade-off between the pulse duration of the reactions and the diffusion strength in the generation of chaos.

In Figure 6E, we show how the pulse duty cycle changes with γ, where we define the duty cycle as the area under the curve during a pulse (when $u > 0$) versus the area under the curve when $u < 0$. The duty cycle scales linearly with γ on a log-log scale up to when γ is approximately 0.2, after which the curve deviates from the linear fit (red line). This deviation coincides with the moment that the system does not completely reach the upper branch of the v nullcline (see insets). It is also at this moment that the system becomes susceptible to chaos and defect formation, which motivates the need to postpone APC/C activation and cyclin degradation such that the M-phase state can be fully reached.

Finally, we examined the influence of the domain size L on the transition to spatial chaos. Figures 6F–6H show that, for fixed values of the diffusion strength and pulse duration ($D = 1$, $\gamma = 1$), spatial chaos is lost when the domain size decreases below a critical value. Figure 6I depicts in further detail how the region of defects and chaos shrinks with decreasing domain sizes. We analyze the critical diffusion strength D that defines the border between chaos/defects (smaller values of D) and continuous trigger waves (larger values of D). Figure 6J shows that the square of this critical diffusion strength (D^2) initially scales linearly with the domain width L and then levels out for large values of L. Thus, larger domains are increasingly susceptible to defect and chaos creation.

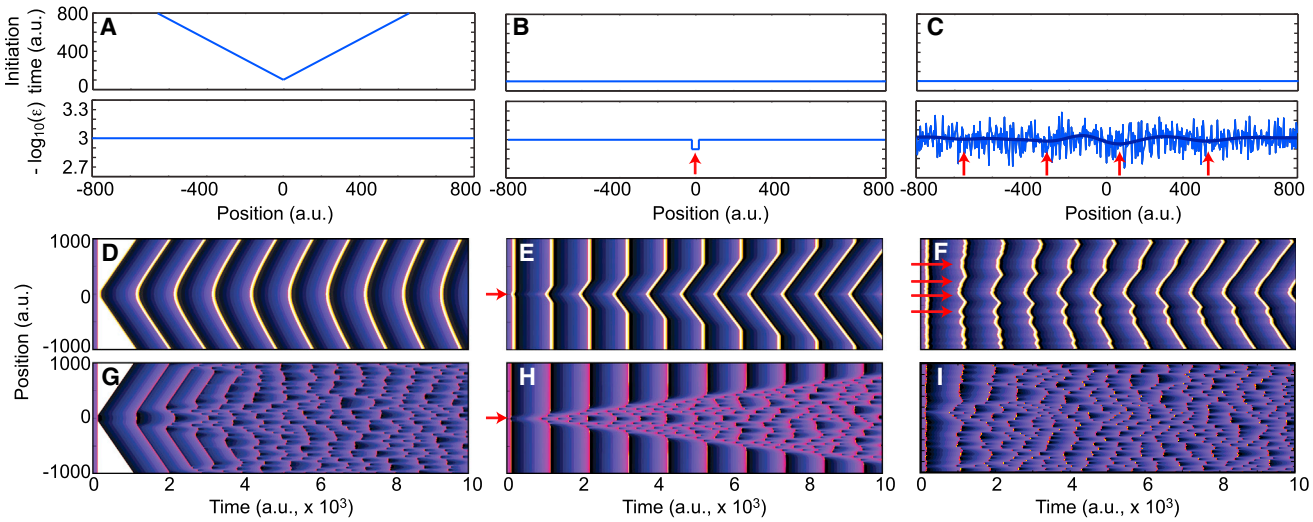

Figure 5. Chaotic Dynamics Are Triggered in the FHN Model by Spatial Heterogeneities

(A–C) Chaotic dynamics in the initial conditions (A) or in the reaction parameters (B and C). In (C), the logarithm of ε, which defines the timescale of the slow variable v, was chosen at random for each discretized point in space from a Gaussian distribution with mean 3 and SD 0.1.

(D–I) Two sets of simulations are shown in the presence of these heterogeneities: first using oscillators with longer pulse duration (D–F), and second using oscillators with short pulse duration (G–I).

To relate these criteria for transitioning into chaos to real physiological values, we review how we can relate the results of cell cycle model 2 (with experimentally measured parameters) presented in Figures 3E and 3H to our generic dimensionless analysis in the FHN model. The diffusion strength D of the relevant proteins involved in the cell cycle is taken to be 10 $\mu m^2/s$, and the period of the cell cycle oscillations in extracts is around 40 min (Yang and Ferrell, 2013). The diameter of a typical *Xenopus laevis* egg is about 1 mm. We assume that the pacemaker region driving the cell cycle and triggering the waves is either the pericentriolar material, with a width of $\sim$1 μm (Chang and Ferrell, 2013; Jackman et al., 2003), or the pronuclei, with diameters $\sim$10 μm. For these physiological parameters, the cell cycle was spatially well coordinated and quasi-synchronous in our simulations (Figure 3H), while an increase in APC/C-dependent degradation by a factor of 10 led to defects and irregular dynamics (Figure 3H). In order to reproduce oscillations of similar period in the FHN model, we can rescale the dimensionless time such that one time unit corresponds to 2 s (while keeping all other parameters in the FHN model the same). The pulse duration can then be adjusted to match the oscillations shown in Figure 3H by setting $\gamma \sim 0.002$ (physiological case) or $\gamma \sim 0.2$ (10-fold increase in APC/C-dependent degradation) (Figure S2).

As one time unit in the FHN model corresponds to 2 s, and we choose one unit of space in the FHN model to be 1 μm, the diffusion coefficient D = 10 $\mu m^2/s$ corresponds to D = 20 in the FHN model. Figure 6D shows that the physiological case (D = 20 and $\gamma \sim 0.002$) is very stable and far away from any irregular dynamics, while the case of a 10-fold increase in APC/C-dependent degradation (D = 20 and $\gamma \sim 0.2$) lies very close to the boundary between continuous trigger waves and irregular dynamics, considering a domain width L = 500. Indeed, in cell cycle model 2, decreasing the domain width 2-fold abolishes the defects and chaos. Similarly, increasing the APC/C-dependent degradation only 5-fold instead of 10-fold (Figure S2G) or increasing the diffusion strength 2-fold (Figure S2H) also prevents defects and chaos from developing. Although it is clear that the FHN model does not capture the finer details of the cell cycle model (such as the exact shape of the nullclines and pulse shape), this simple back-of-the-envelope calculation shows that many results can still be gleaned from a generic analysis using the FHN model. Thus, for the FHN model, as was the case for cell cycle model 2, spatial chaos becomes possible at parameter values that are not far from physiological values.

DISCUSSION

We began by testing the hypothesis of McIsaac et al. that slowing down the fertilization-initiated calcium wave would lead to spatio-temporal chaos (Figure 1) (McIsaac et al., 2011). We showed experimentally that varying temperature can slow down the calcium wave and used this approach to test whether normal development depends on a rapid initial calcium wave. Cell cycle oscillations proceeded normally, and healthy tadpoles developed even when the speed of the calcium wave was reduced by a factor of $\sim$2 (Figure 2).

To understand where the discrepancy lay between the model and the experimental system, we carried out simulations of various relaxation oscillator models and found that chaos emerged only when the oscillatory reactions were sufficiently short in pulse duration (Figures 3 and 4). A variety of heterogeneities, including differences in the initial conditions or in the reaction parameters, were found to trigger such chaos (Figure 5), and the transition into chaos sometimes spread in a trigger wave-like fashion through a homogeneous medium (Figure 5). Similar

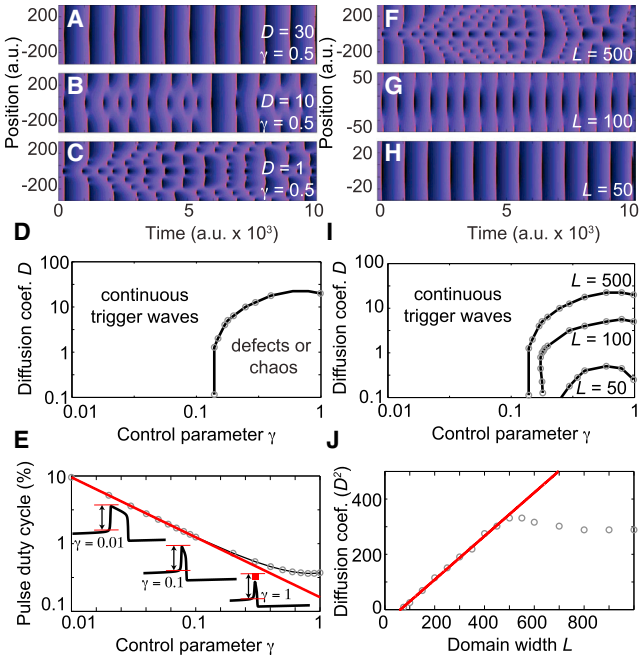

Figure 6. Decreasing Pulse Duration, Decreasing Diffusion Strength, and Increasing Domain Widths Promote Defects and Chaotic Dynamics

(A–C) The transition into chaos when varying the diffusion strength D (with control parameter $\gamma = 0.5$) in the FHN reaction. $D = 30$ (A), $D = 10$ (B), and $D = 1$ (C). The simulations show the dynamics in the presence of a central pacemaker region (as in Figures 5E and 5F).

(D) Two characteristic dynamical regimes are found as a function of γ and D: continuous trigger waves, and defects or chaotic dynamics.

(E) The pulse duty cycle (percentage of the time $u > 0$) initially varies linearly with the control parameter γ (in $\log_{10}$ scale) but then deviates as γ increases further, and the pulse no longer reaches the upper branch of the u nullcline.

(F–H) The stabilization when decreasing the domain width L (with $D = \gamma = 1$). $L = 500$ (F), $L = 100$ (G), and $L = 50$ (H).

(I) The boundary between continuous trigger waves and defects or chaos shifts with the domain width L.

(J) The critical diffusion coefficient at the boundary shown in (I) initially scales linearly with L (for $\gamma = 1$) but becomes constant for large values of L.

results were found in simulations with two spatial dimensions (Figure S3).

Since our experiments showed no sign of chaos when the calcium wave was slowed, and moreover frog cytoplasm is likely to contain the sorts of heterogeneities that can trigger chaos, we propose that the reactions of the *Xenopus* cell cycle oscillator do not generate pulses in short enough duration to admit chaos. Although it is difficult to experimentally determine exactly how short the duration of M phase is, because experiments are done on embryos and extracts whose volumes are sufficiently large that they are far from the well-stirred limit, these conclusions are consistent with past experimental work (Pomerening et al., 2005; Solomon et al., 1990; Tsai et al., 2014; Yang and Ferrell, 2013).

In other biological systems, reaction dynamics with short pulse durations may in fact be present. One example is cardiac dynamics, where abrupt depolarization of the myocyte is important for normal force/velocity relationships and cardiac contractility. In a system like this, chaos might be an important hazard. The FHN equations have in fact been widely used to model heart conduction, and some arrhythmias have been interpreted as chaotic modes of the underlying spatio-temporal dynamics (Babloyantz, 1994; Chialvo and Jalife, 1987; Duckett and Barkley, 2000; Rappel et al., 1999; Starmer et al., 1993; Tyson and Keener, 1988; van der Pol and van der Mark, 1928; Winfree, 1989). Another related example is the complex chaotic (tent) patterns of pigment that are found on the shells of some mollusks (Meinhardt, 2003). Such mollusk patterns have been modeled using cellular automata (Wolfram, 1984) and reaction-diffusion equations (Ermentrout et al., 1986; Meinhardt and Klingler, 1987). In this case, the complex beautiful dynamics of the spatially chaotic system may be a feature of the system that has been selected for rather than a hazard to be avoided.

EXPERIMENTAL PROCEDURES

Xenopus Experiments

All animal work was conducted according to relevant national and international guidelines. Animal protocols were approved by the Stanford University Administrative Panel on Laboratory Animal Care. Female *Xenopus laevis* frogs were induced by human chorionic gonadotropin injection, and pelvic massage was performed to collect eggs 12 to 20 hr after induction. In vitro fertilization was performed in the device shown in Figure 2A by mixing eggs with smashed testes for 1 min in several drops of 0.1× Marc's modified Ringer's (MMR) buffer. The MMR buffer was first brought to the temperature of interest before fertilization of the eggs. The embryonic divisions were imaged with a stereoscope Nikon SMZ 1500 with a Leica DFC425 camera. Frame rate was 1 frame/30 s to image the long-term development and 1 frame/10 s to image the calcium wave.

Mathematical Models

Here, we briefly discuss the origin and variables involved in the different models used throughout this work. The full set of equations, the parameters used, and the details of each numerical simulation can be found in the Supplemental Information.

Cell Cycle Model 1

This cell cycle model, used in McIsaac et al. (2011) (and introduced before in Pomerening et al., 2003, 2005), consists of nine ODEs, representing the different phosphorylation states of the cyclin-B-Cdk1 complex and the activities of cyclin-B, Cdc25, Wee1, Plx1, and APC/C.

Cell Cycle Model 2

This cell cycle model, introduced in Yang and Ferrell (2013), consists of two ODEs. The first ODE describes the activity of Cdk1, and the second ODE describes the synthesis and destruction of the mitotic cyclins.

Asymmetric FHN Model

The general FHN model (Fitzhugh, 1961; Nagumo et al., 1964) was adjusted to allow for tuning of the sharpness of the relaxation oscillations. An additional parameter γ was introduced that changes the timescale of the evolution of the v variable.

SUPPLEMENTAL INFORMATION

Supplemental Information includes Supplemental Experimental Procedures, numerical methods and initialization of simulations, three figures, and three movies and can be found with this article online at http://dx.doi.org/10.1016/j.celrep.2015.06.070.

AUTHOR CONTRIBUTIONS

L.G. and J.E.F. designed the study. L.G. and K.C.H. performed the computational analyses. L.G. performed the *Xenopus* experiments. L.G., K.C.H., and J.E.F. wrote the manuscript and contributed to the ideas through discussions.

Please cite this article in press as: Gelens et al., How Does the *Xenopus laevis* Embryonic Cell Cycle Avoid Spatial Chaos?, Cell Reports (2015), http://dx.doi.org/10.1016/j.celrep.2015.06.070

ACKNOWLEDGMENTS

We thank Lauren Chircus, who carried out preliminary experiments for this study, and Thomas Erneux, Graham Anderson, and the J.E.F. lab for helpful comments and discussions. This work was supported by NIH grants GM046383 and GM107615 (to J.E.F.) and DP2-OD006466 (to K.C.H.). K.C.H. and J.E.F. also acknowledge support from the Stanford Systems Biology Center, funded by NIH grant P50 GM107615. L.G. acknowledges support by the Research Foundation-Flanders, the Belgian American Educational Foundation, and the Research Council of the Vrije Universiteit Brussel.

Received: January 26, 2015
Revised: April 13, 2015
Accepted: June 24, 2015
Published: July 23, 2015

REFERENCES

Babloyantz, A. (1994). Mechanisms of target and spiral wave propagation in single cells. Chaos *4*, 473–476.

Bonnet, J., Coopman, P., and Morris, M.C. (2008). Characterization of centrosomal localization and dynamics of Cdc25C phosphatase in mitosis. Cell Cycle *7*, 1991–1998.

Booth, V., and Erneux, T. (1995). Understanding propagation failure as a slow capture near a limit-point. SIAM J. Appl. Math. *55*, 1372–1389.

Bub, G., Shrier, A., and Glass, L. (2002). Spiral wave generation in heterogeneous excitable media. Phys. Rev. Lett. *88*, 058101.

Busa, W.B., and Nuccitelli, R. (1985). An elevated free cytosolic Ca2+ wave follows fertilization in eggs of the frog, Xenopus laevis. J. Cell Biol. *100*, 1325–1329.

Chang, J.B., and Ferrell, J.E., Jr. (2013). Mitotic trigger waves and the spatial coordination of the Xenopus cell cycle. Nature *500*, 603–607.

Chialvo, D.R., and Jalife, J. (1987). Non-linear dynamics of cardiac excitation and impulse propagation. Nature *330*, 749–752.

Deng, B. (1991). The existence of infinitely many traveling front and back waves in the FitzHugh-Nagumo equations. SIAM J. Appl. Math. *22*, 1631–1650.

Duckett, G., and Barkley, D. (2000). Modeling the dynamics of cardiac action potentials. Phys. Rev. Lett. *85*, 884–887.

Ermentrout, G.B., and Rinzel, J. (1996). Reflected waves in an inhomogeneous excitable medium. SIAM J. Appl. Math. *56*, 1107–1128.

Ermentrout, B., Campbell, J., and Oster, G. (1986). A model for shell patterns based on neural activity. Veliger *28*, 369–388.

Fitzhugh, R. (1961). Impulses and physiological states in theoretical models of nerve membrane. Biophys. J. *1*, 445–466.

Fontanilla, R.A., and Nuccitelli, R. (1998). Characterization of the sperm-induced calcium wave in Xenopus eggs using confocal microscopy. Biophys. J. *75*, 2079–2087.

Gelens, L., Anderson, G.A., and Ferrell, J.E., Jr. (2014). Spatial trigger waves: positive feedback gets you a long way. Mol. Biol. Cell *25*, 3486–3493.

Gerhart, J. (1980). Mechanisms regulating pattern formation in the amphibian egg and early embryo. In Biological Regulation and Development, R.F. Goldberger, ed. (Springer US), pp. 133–316.

Goldbeter, A. (1993). Modeling the mitotic oscillator driving the cell division cycle. Comments Theor. Biol. *3*, 75–107.

Hall, K., and Glass, L. (1999). How to tell a target from a spiral: The two probe problem. Phys. Rev. Lett. *82*, 5164–5167.

Hausen, P., and Riebesell, P. (1991). The early development of Xenopus laevis: an atlas of the histology (Berlin: Springer Verlag).

Hoffmann, I., Clarke, P.R., Marcote, M.J., Karsenti, E., and Draetta, G. (1993). Phosphorylation and activation of human cdc25-C by cdc2–cyclin B and its involvement in the self-amplification of MPF at mitosis. EMBO J. *12*, 53–63.

Jackman, M., Lindon, C., Nigg, E.A., and Pines, J. (2003). Active cyclin B1-Cdk1 first appears on centrosomes in prophase. Nat. Cell Biol. *5*, 143–148.

Keldermann, R.H., Nash, M.P., and Panfilov, A.V. (2007). Pacemakers in a reaction-diffusion mechanics system. J. Stat. Phys. *128*, 375–392.

Kim, S.Y., and Ferrell, J.E., Jr. (2007). Substrate competition as a source of ultrasensitivity in the inactivation of Wee1. Cell *128*, 1133–1145.

King, R.W., Deshaies, R.J., Peters, J.M., and Kirschner, M.W. (1996). How proteolysis drives the cell cycle. Science *274*, 1652–1659.

Li, Y.-X. (2003). Tango waves in a bidomain model of fertilization calcium waves. Physica D *186*, 27–49.

McGowan, C.H., and Russell, P. (1993). Human Wee1 kinase inhibits cell division by phosphorylating p34cdc2 exclusively on Tyr15. EMBO J. *12*, 75–85.

McIsaac, R.S., Huang, K.C., Sengupta, A., and Wingreen, N.S. (2011). Does the potential for chaos constrain the embryonic cell-cycle oscillator? PLoS Comput. Biol. *7*, e1002109.

Meinhardt, H. (2003). The Algorithmic Beauty of Sea Shells, Third Edition (Heidelberg: Springer).

Meinhardt, H., and Klingler, M. (1987). A model for pattern-formation on the shells of molluscs. J. Theor. Biol. *126*, 63–89.

Minshull, J., Blow, J.J., and Hunt, T. (1989). Translation of cyclin mRNA is necessary for extracts of activated xenopus eggs to enter mitosis. Cell *56*, 947–956.

Mueller, P.R., Coleman, T.R., and Dunphy, W.G. (1995a). Cell cycle regulation of a Xenopus Wee1-like kinase. Mol. Biol. Cell *6*, 119–134.

Mueller, P.R., Coleman, T.R., Kumagai, A., and Dunphy, W.G. (1995b). Myt1: a membrane-associated inhibitory kinase that phosphorylates Cdc2 on both threonine-14 and tyrosine-15. Science *270*, 86–90.

Murray, A.W., and Kirschner, M.W. (1989). Cyclin synthesis drives the early embryonic cell cycle. Nature *339*, 275–280.

Nagumo, J., Arimoto, S., and Yoshizawa, S. (1964). An active pulse transmission line simulating nerve axon. Proc. IRE *50*, 2061–2070.

Novak, B., and Tyson, J.J. (1993a). Modeling the cell division cycle: M-phase trigger, oscillations, and size control. J. Theor. Biol. *165*, 101–134.

Novak, B., and Tyson, J.J. (1993b). Numerical analysis of a comprehensive model of M-phase control in Xenopus oocyte extracts and intact embryos. J. Cell Sci. *106*, 1153–1168.

Panfilov, A.V., Keldermann, R.H., and Nash, M.P. (2005). Self-organized pacemakers in a coupled reaction-diffusion-mechanics system. Phys. Rev. Lett. *95*, 258104.

Parker, L.L., and Piwnica-Worms, H. (1992). Inactivation of the p34cdc2-cyclin B complex by the human WEE1 tyrosine kinase. Science *257*, 1955–1957.

Pomerening, J.R., Sontag, E.D., and Ferrell, J.E., Jr. (2003). Building a cell cycle oscillator: hysteresis and bistability in the activation of Cdc2. Nat. Cell Biol. *5*, 346–351.

Pomerening, J.R., Kim, S.Y., and Ferrell, J.E., Jr. (2005). Systems-level dissection of the cell-cycle oscillator: bypassing positive feedback produces damped oscillations. Cell *122*, 565–578.

Prat, A., and Li, Y.-X. (2003). Stability of front solutions in inhomogeneous media. Physica D *186*, 50–68.

Rabinovitch, A., Aviram, I., Gulko, N., and Ovsyshcher, E. (1999). A Model for the Propagation of Action Potentials in Non-Uniformly Excitable Media. J. Theor. Biol. *196*, 141–154.

Rappel, W.J., Fenton, F., and Karma, A. (1999). Spatiotemporal control of wave instabilities in cardiac tissue. Phys. Rev. Lett. *83*, 456–459.

Romond, P.C., Rustici, M., Gonze, D., and Goldbeter, A. (1999). Alternating oscillations and chaos in a model of two coupled biochemical oscillators driving successive phases of the cell cycle. Ann. N Y Acad. Sci. *879*, 180–193.

Sha, W., Moore, J., Chen, K., Lassaletta, A.D., Yi, C.S., Tyson, J.J., and Sible, J.C. (2003). Hysteresis drives cell-cycle transitions in Xenopus laevis egg extracts. Proc. Natl. Acad. Sci. USA *100*, 975–980.

Solomon, M.J., Glotzer, M., Lee, T.H., Philippe, M., and Kirschner, M.W. (1990). Cyclin activation of p34cdc2. Cell *63*, 1013–1024.

Sridhar, S., Sinha, S., and Panfilov, A.V. (2010). Anomalous drift of spiral waves in heterogeneous excitable media. Phys. Rev. E Stat. Nonlin. Soft Matter Phys. *82*, 051908.

Starmer, C.F., Biktashev, V.N., Romashko, D.N., Stepanov, M.R., Makarova, O.N., and Krinsky, V.I. (1993). Vulnerability in an excitable medium: analytical and numerical studies of initiating unidirectional propagation. Biophys. J. *65*, 1775–1787.

Steinberg, B.E., Glass, L., Shrier, A., and Bub, G. (2006). The role of heterogeneities and intercellular coupling in wave propagation in cardiac tissue. Philos. Trans. A Math. Phys. Eng. Sci. *364*, 1299–1311.

Tang, Z., Coleman, T.R., and Dunphy, W.G. (1993). Two distinct mechanisms for negative regulation of the Wee1 protein kinase. EMBO J. *12*, 3427–3436.

Trunnell, N.B., Poon, A.C., Kim, S.Y., and Ferrell, J.E., Jr. (2011). Ultrasensitivity in the Regulation of Cdc25C by Cdk1. Mol. Cell *41*, 263–274.

Tsai, T.Y., Theriot, J.A., and Ferrell, J.E., Jr. (2014). Changes in oscillatory dynamics in the cell cycle of early Xenopus laevis embryos. PLoS Biol. *12*, e1001788.

Tyson, J.J., and Keener, J.P. (1988). Singular perturbation-theory of traveling waves in excitable media. Physica D *32*, 327–361.

van der Pol, B., and van der Mark, J. (1928). The heartbeat considered as a relaxation oscillator, and an electrical model of the heart. London, Edinburgh and Dublin Physiological Magazine and Journal of Science *6* (*Supp*), 763–775.

Vinod, P.K., Zhou, X., Zhang, T., Mayer, T.U., and Novak, B. (2013). The role of APC/C inhibitor Emi2/XErp1 in oscillatory dynamics of early embryonic cell cycles. Biophys. Chem. *177-178*, 1–6.

Winfree, A.T. (1989). Electrical instability in cardiac muscle: phase singularities and rotors. J. Theor. Biol. *138*, 353–405.

Wolfram, S. (1984). Cellular automata as models of complexity. Nature *311*, 419–424.

Yang, Q., and Ferrell, J.E., Jr. (2013). The Cdk1-APC/C cell cycle oscillator circuit functions as a time-delayed, ultrasensitive switch. Nat. Cell Biol. *15*, 519–525.

Zhou, Y., and Bell, J. (1994). Study of propagation along nonuniform excitable fibers. Math. Biosci. *119*, 169–203.

Cell Reports

Supplemental Information

How Does the *Xenopus laevis* Embryonic Cell Cycle Avoid Spatial Chaos?

Lendert Gelens, Kerwyn Casey Huang, and James E. Ferrell, Jr.

Inventory of Supplemental Information.

1. Supplemental Data.
The Supplemental Data document contains three supplemental figures (Figures S1-S3):

1.1. Figure S1, Related to Figure 1.
Small differences in initial conditions lead to different dynamical outputs.

1.2. Figure S2, Related to Figure 6.
Relating physiological parameters of cell cycle model 2 to the FHN model.

1.3. Figure S3, Related to Figure 5.
FHN dynamics in two spatial dimensions.

2. Supplemental Experimental Procedures.

This part contains details of how we implemented the two cell cycle models (2.1-2.2), the asymmetrical FitzHugh-Nagumo model (2.3), and the diffusive spatial coupling (2.4).

3. Numerical methods and initialization of simulations.

In this part we present details of the numerical methods and initializations for the simulations shown in the main text Figures.

4. Supplemental Movies.

4.1. Movie S1, Related to Figure 2.
Rapid fertilization waves in embryos fertilized at 23°C. The movie lasts for 20 min and the frame rate used was 1 frame every 10 s.

4.2. Movie S2, Related to Figure 2.
Slower fertilization waves in embryos fertilized at 13°C. The movie lasts for 20 min and the frame rate used was 1 frame every 10 s.

4.3. Movie S3, Related to Figure 2.
Normal development in embryos fertilized at either 13°C or 23°C and then allowed to develop at 23°C. One batch of eggs was fertilized at 13°C and then returned to 23°C after the calcium wave had passed (20 min after fertilization). A second batch of eggs from the same frog was fertilized at 23°C at the same time and always maintained at 23°C. The movie starts 28 min after fertilization and continues up to approximately 33 h after fertilization. One frame was taken every 30 s. The second part of the movie is played 5 times faster as indicated.

5. Supplemental References.

1. Supplemental Data

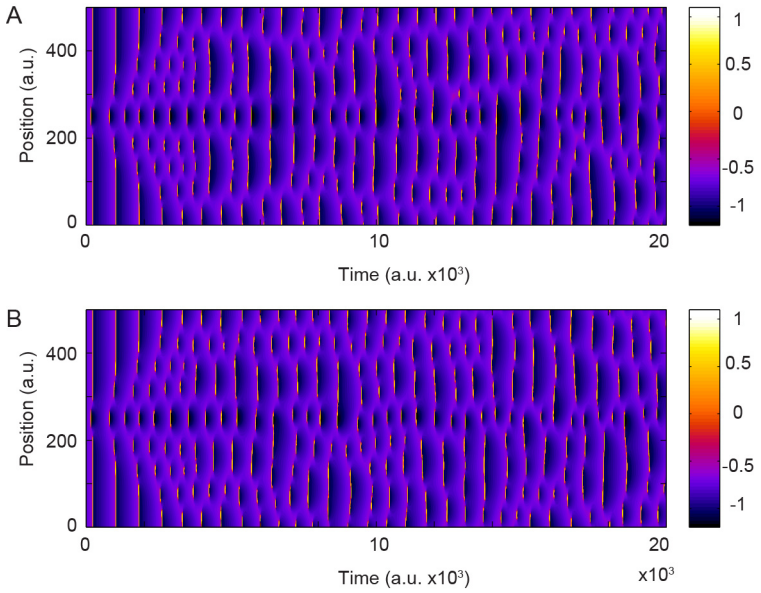

Figure S1: Small differences in initial conditions lead to different dynamical outputs. FHN model with $D = 1$ and $\gamma = 1$, with the middle region oscillating faster ($b = 0.5$) than the outer regions ($b = 1$). (A) The time evolution for initial conditions ($u = -0.7, v = -0.32$). (B) The time evolution for initial conditions ($u = -0.8, v = -0.32$).

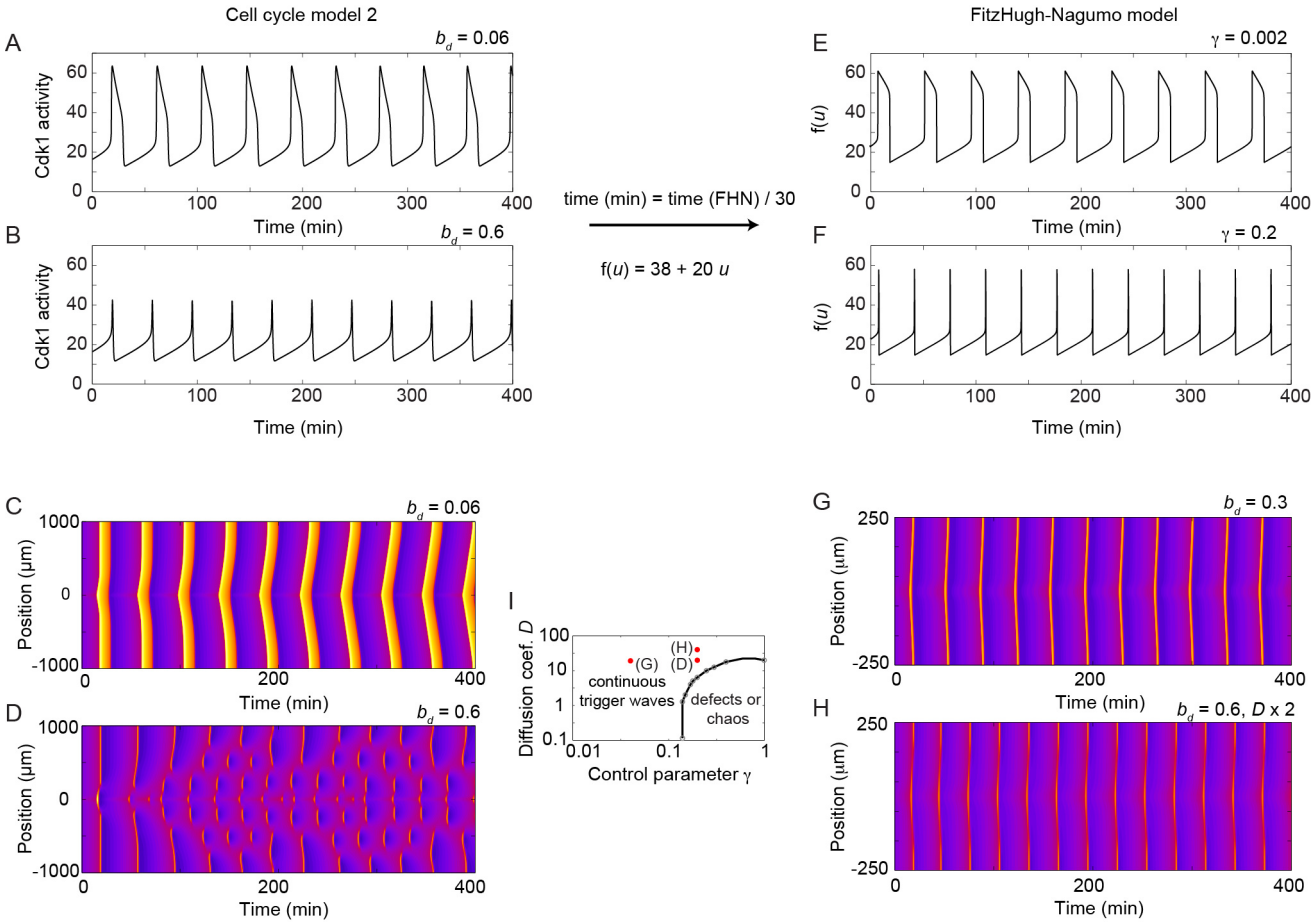

Figure S2: Relating physiological parameters of cell cycle model 2 to the FHN model. Simulations showing cell cycle oscillations obtained in cell cycle model 2 for $b_d = 0.06$ (A) and $b_d = 0.6$ (B). The corresponding spatio-temporal dynamics in the presence of a central pacemaker region are shown in (C,D). Using an appropriate rescaling of time and u, the FHN model produces similar oscillations (E,F). Simulations of cell cycle model 2 show that decreasing the degradation rate twofold $b_d = 0.3$ (G), or increasing the diffusion coefficient twofold (H), both abolish irregular dynamics in favor of continuous trigger wave dynamics. Such dynamics is consistent with the analysis of the FHN model in Figure 6. Figure 6D is repeated in panel (I) where red dots indicate the dimensionless parameters corresponding to the simulations in panel (D),(G), and (H).

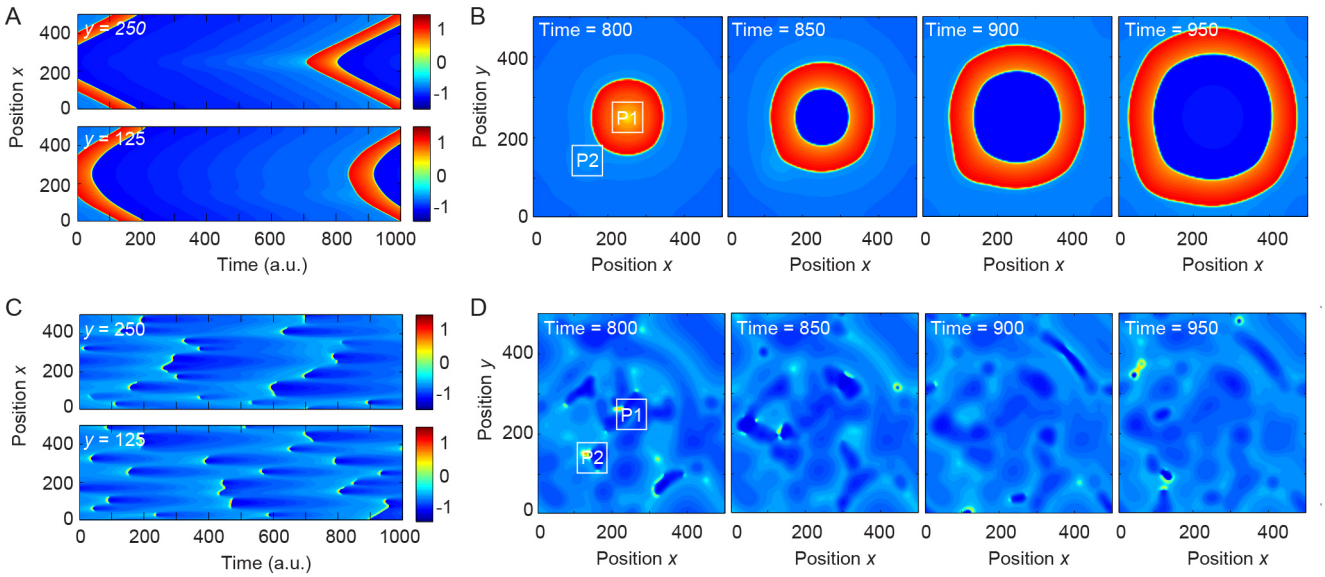

Figure S3: FHN dynamics in two spatial dimensions. The dynamics is shown of spatially coupled oscillators with long (A,B, $\gamma = 0.01$) and short (C,D, $\gamma = 1$) pulse durations in two spatial dimensions. Two pacemaker regions with faster oscillation periods (P1 and P2) and a noisy variation of the period were introduced. (A,C) The evolution over time across x position at two fixed y positions. (B,D) Snapshots of the whole 2D space at different times.

1.1. Figure S1, Related to Figure 1: Small differences in initial conditions lead to different dynamical outputs

We simulated the spatiotemporal evolution of u using the FHN model for two slightly different initial conditions: (A) ($u = -0.7$, $v = -0.32$), and (B) ($u = -0.8, v = -0.32$). The parameters in the FHN model were chosen to be $\gamma = 1$, $D = 1$, $a = 0$, and $b = 1$ everywhere, except in a central region of width 40 where $b = 0.5$. $N = 500$ discretization points were used, and the domain width was $L = 500$. The discretization time step was $\delta t = 0.01$. One can see that although in both cases the dynamics are initially very similar, the behaviors increasingly differ as time proceeds. Such sensitivity to initial conditions is a typical consequence of chaotic dynamics.

1.2. Figure S2, Related to Figure 6: Relating physiological parameters of cell cycle model 2 to the FHN model

Figure S2A,B show the cell cycle oscillations obtained with cell cycle model 2 with the standard set of parameters, except the cyclin degradation rate due to APC/C activity was set to $b_d = 0.06$ in (A) and $b_d = 0.6$ in (B), similar to Figure 3E. We define a central pacemaker region of width 40 in a domain of size $L = 2000$ μm. This pacemaker region has $a_{cdc} = 0.9$, while in the rest of space $a_{cdc} = 0.8$. Simulating the time evolution using a discretization time step of $\delta t = 0.01$ and $N = 2000$ spatial discretization points, we find continuous trigger waves for $b_d = 0.06$ (C), and irregular dynamics for $b_d = 0.6$ (D). This shows that heterogeneities generated by a calcium wave (Figure 3H) and by a pacemaker region (C,D) produce similar dynamics.

To relate these dynamics to the analysis presented in Figure 6 for the dimensionless FHN model, we need to relate the physiological values of cell cycle model 2 to the parameters and variables in the FHN model. (E,F) show how rescaling time, rescaling the variable u, and adjusting the value of γ can produce similar oscillations as in cell cycle model 2. In order to compare spatio-temporal dynamics, we use this rescaled time and choose one unit of space in the FHN model to be 1 μm. As such, the diffusion coefficient $D = 10$ μm^2/s corresponds to $D = 20$ of cell cycle model 2 in light of the FHN model. In this manner, we can use Figure 6D to interpret the predicted spatiotemporal dynamics in the FHN model. For $(\gamma, D) = (0.002, 20)$, the FHN model predicts continuous trigger waves, which is indeed the case in (C). For a domain size $L = 500$, the parameter set (γ,D) = (0.2,20) is very close to the boundary between continuous trigger waves and defects/chaos. Simulations using cell cycle model 2 in a domain with $L = 500$ still show similar irregular dynamics as in (D). However, decreasing the degradation rate twofold to $b_d = 0.3$ (corresponding to decreasing γ in the FHN model) restores the continuous trigger wave dynamics (G). Similarly, by increasing the diffusion coefficient twofold, continuous trigger wave dynamics are also recovered (H). Finally, decreasing the domain width L twofold has the same stabilizing effect, showing that cell cycle model 2 indeed operates close to the boundary between continuous trigger wave dynamics and defects/chaos when $(b_d, D) = (0.6, 10$ μm^2/s), as predicted by the analysis of the FHN model in Figure 6.

1.3. Figure S3, Related to Figure 5: FHN dynamics in two spatial dimensions

We examined whether the observed chaotic dynamics also persisted in two spatial dimensions, and whether they were again regulated by the pulse duration of the oscillatory reactions. We introduced spatial heterogeneity by choosing one central region that oscillates fastest (Pacemaker 1 - P1), a second region that oscillates more slowly than P1 (Pacemaker 2 - P2), and the rest of space oscillating on average slower than either pacemaker region. Smaller amounts of noisy variation of the oscillation period in space were also introduced.

Dynamics were studied in a square, with $N = 128$ spatial discretization points along each dimension, which were of size $L = 500$. The discretization time step was $\delta t = 0.01$. The system dynamics were recorded every time unit over 1000 time units, after an initial transient of 3000 time units. In a box at the center of the square (P1) with a width and height of 20 discretization points, the value of ε was $-\log_{10}(\varepsilon) = \rho$, where ρ was randomly chosen at each discretization point from a Gaussian distribution with mean 2.9 and standard deviation 0.02. Similarly, in a box (P2) with a width and height of 20 discretization points centered around $(x, y) = (125, 125)$, the value of ε was $-\log_{10}(\varepsilon) = \rho$, where ρ was randomly chosen at each discretization point from a Gaussian distribution with mean 2.95 and standard deviation 0.02. In the remainder of the space, the value of ε was $-\log_{10}(\varepsilon) = \rho$, where ρ was randomly chosen at each discretization point from a Gaussian distribution with mean 3 and standard deviation 0.02. In (A,B) $\gamma = 0.01$, while in (C,D) $\gamma = 1$.

In simulations of oscillators with longer pulse duration coupled in space, P1 dominated the whole space by emitting regular target waves that spread out and set the pace (Figure S3A,B). For large values of γ that give rise to oscillations with short pulses, chaotic dynamics set in and caused small regions in space to spike and

form a small target wave that spread out over short distances before breaking up and disappearing (Figure S3C,D).

2. Supplemental Experimental Procedures

In this Section we provide a detailed description of the mathematical models used to describe the biochemical reaction dynamics, as well as the numerical methods used to produce each Figure.

2.1. Cell cycle model 1

This cell cycle model, previously used in Ref. (McIsaac et al., 2011) and originally introduced in Refs. (Pomerening et al., 2003; Pomerening et al., 2005), consists of 9 ordinary differential equations (ODEs). One ODE models the dynamics of cyclin B, and 4 ODEs are used to describe the different phosphorylated/ dephosphorylated states of the cyclin B-Cdk1 complex. The cyclin B-Cdk1-Tp complex is the enzymatically active form. Cyclin B-Cdk1-Tp is assumed to activate the polo-like kinase (Plx1_{act}). Plx1_{act} then phosphorylates and activates the anaphase-promoting complex (APC_{act}), which polyubiquitinates cyclin B, tagging it for degradation by the proteosome. Dual positive-feedback loops are achieved through cyclin B-Cdk1-Tp-mediated activation of the Tyr-15 phosphatase ($\text{Cdc25}_{\text{act}}$) and Cyclin B-Cdk1-Tp-mediated inactivation of the Tyr-15 kinase (Wee1_{act}). The 9 ODEs are as follows:

$$\begin{aligned}
\frac{d[\text{cyclin B}]}{dt} &= k_s - k_{\text{dest}}[\text{APC}]_{\text{act}}[\text{cyclin B}] \qquad (1)\\
&\quad -k_a([\text{Cdk1}]_{\text{tot}} - [\text{cyclin B-Cdk1}] - [\text{cyclin B-Cdk1-Yp}]\\
&\quad -[\text{cyclin B-Cdk1-YpTp}] - [\text{cyclin B-Cdk1-Tp}])[\text{cyclin B}] + k_d[\text{cyclin B-Cdk1}]\\
\frac{d[\text{cyclin B-Cdk1}]}{dt} &= k_a([\text{Cdk1}]_{\text{tot}} - [\text{cyclin B-Cdk1}] - [\text{cyclin B-Cdk1-Yp}] \qquad (2)\\
&\quad -[\text{cyclin B-Cdk1-YpTp}] - [\text{cyclin B-Cdk1-Tp}])[\text{cyclin B}] - k_d[\text{cyclin B-Cdk1}]\\
&\quad -k_{\text{dest}}[\text{APC}]_{\text{act}}[\text{cyclin B-Cdk1}]\\
&\quad -k_{\text{wee1}}[\text{Wee1}]_{\text{act}}[\text{cyclin B-Cdk1}]\\
&\quad -k_{\text{wee1,basal}}([\text{Wee1}]_{\text{tot}} - [\text{Wee1}]_{\text{act}})[\text{cyclin B-Cdk1}]\\
&\quad +k_{\text{cdc25}}[\text{Cdc25}]_{\text{act}}[\text{cyclin B-Cdk1-Yp}]\\
&\quad +k_{\text{cdc25,basal}}([\text{Cdc25}]_{\text{tot}} - [\text{Cdc25}]_{\text{act}})[\text{cyclin B-Cdk1-Yp}]\\
\frac{d[\text{cyclin B-Cdk1-Yp}]}{dt} &= k_{\text{wee1}}[\text{Wee1}]_{\text{act}}[\text{cyclin B-Cdk1}] \qquad (3)\\
&\quad +k_{\text{wee1,basal}}([\text{Wee1}]_{\text{tot}} - [\text{Wee1}]_{\text{act}})[\text{cyclin B-Cdk1}]\\
&\quad -k_{\text{cdc25}}[\text{Cdc25}]_{\text{act}}[\text{cyclin B-Cdk1-Yp}] - k_{\text{cdc25,basal}}([\text{Cdc25}]_{\text{tot}} - [\text{Cdc25}]_{\text{act}})\\
&\quad [\text{cyclin B-Cdk1-Yp}] - k_{\text{cak}}[\text{cyclin B-Cdk1-Yp}] + k_{\text{pp2c}}[\text{cyclin B-Cdk1-YpTp}]\\
&\quad -k_{\text{dest}}[\text{APC}]_{\text{act}}[\text{cyclin B-Cdk1-Yp}]\\
\frac{d[\text{cyclin B-Cdk1-YpTp}]}{dt} &= k_{\text{cak}}[\text{cyclin B-Cdk1-Yp}] - k_{\text{pp2c}}[\text{cyclin B-Cdk1-YpTp}] \qquad (4)\\
&\quad -k_{\text{cdc25}}[\text{Cdc25}]_{\text{act}}[\text{cyclin B-Cdk1-YpTp}] - k_{\text{cdc25,basal}}([\text{Cdc25}]_{\text{tot}}\\
&\quad -[\text{Cdc25}]_{\text{act}})[\text{cyclin B-Cdk1-YpTp}] + k_{\text{wee1}}[\text{Wee1}]_{\text{act}}[\text{cyclin B-Cdk1-Tp}]\\
&\quad +k_{\text{wee1,basal}}([\text{Wee1}]_{\text{tot}} - [\text{Wee1}]_{\text{act}})[\text{cyclin B-Cdk1-Tp}]\\
&\quad -k_{\text{dest}}[\text{APC}]_{\text{act}}[\text{cyclin B-Cdk1-YpTp}]\\
\frac{d[\text{cyclin B-Cdk1-Tp}]}{dt} &= k_{\text{cdc25}}[\text{Cdc25}]_{\text{act}}[\text{cyclin B-Cdk1-YpTp}] \qquad (5)\\
&\quad +k_{\text{cdc25,basal}}([\text{Cdc25}]_{\text{tot}} - [\text{Cdc25}]_{\text{act}})[\text{cyclin B-Cdk1-YpTp}]\\
&\quad -k_{\text{wee1}}[\text{Wee1}]_{\text{act}}[\text{cyclin B-Cdk1-Tp}] - k_{\text{wee1,basal}}([\text{Wee1}]_{\text{tot}} - [\text{Wee1}]_{\text{act}})\\
&\quad [\text{cyclin B-Cdk1-Tp}] - k_{\text{dest}}[\text{APC}]_{\text{act}}[\text{cyclin B-Cdk1-Tp}]\\
\frac{d[\text{Cdc25}]_{\text{act}}}{dt} &= k_{\text{cdc25,on}}\left(\frac{[\text{cyclin B-Cdk1-Tp}]^{n_{\text{cdc25}}}}{(\text{EC50})_{\text{cdc25}}^{n_{\text{cdc25}}} + [\text{cyclin B-Cdk1-Tp}]^{n_{\text{cdc25}}}}\right) \qquad (6)\\
&\quad \times([\text{Cdc25}]_{\text{tot}} - [\text{Cdc25}]_{\text{act}}) - k_{\text{cdc25,off}}[\text{Cdc25}]_{\text{act}}
\end{aligned}$$

$$\frac{d[\text{Wee1}]_{\text{act}}}{dt} = -k_{\text{wee1,off}}\left(\frac{[\text{cyclin B-Cdk1-Tp}]^{n_{\text{wee1}}}}{(\text{EC50})^{n_{\text{wee1}}}_{\text{wee1}} + [\text{cyclin B-Cdk1-Tp}]^{n_{\text{wee1}}}}\right) \times [\text{Wee1}]_{\text{act}} + k_{\text{wee1,on}}([\text{Wee1}]_{\text{tot}} - [\text{Wee1}]_{\text{act}}) \quad (7)$$

$$\frac{d[\text{Plx1}]_{\text{act}}}{dt} = k_{\text{plx1,on}}\left(\frac{[\text{cyclin B-Cdk1-Tp}]^{n_{\text{plx1}}}}{(\text{EC50})^{n_{\text{plx1}}}_{\text{plx1}} + [\text{cyclin B-Cdk1-Tp}]^{n_{\text{plx1}}}}\right) \times ([\text{Plx1}]_{\text{tot}} - [\text{Plx1}]_{\text{act}}) - k_{\text{plx1,off}}[\text{Plx1}]_{\text{act}} \quad (8)$$

$$\frac{d[\text{APC}]_{\text{act}}}{dt} = k_{\text{APC,on}}\left(\frac{[\text{Plx1}]^{n_{\text{APC}}}_{\text{act}}}{(\text{EC50})^{n_{\text{APC}}}_{\text{APC}} + [\text{Plx1}]^{n_{\text{APC}}}_{\text{act}}}\right) \times ([\text{APC}]_{\text{tot}} - [\text{APC}]_{\text{act}}) - k_{\text{APC,off}}[\text{APC}]_{\text{act}} \quad (9)$$

Following Ref. (McIsaac et al., 2011), the standard parameter set that we used throughout our study (unless mentioned otherwise), is the following:

$$\begin{aligned}
k_s &= 0.02\ \text{s}^{-1} \\
k_{\text{dest}} &= 0.01\ \text{s}^{-1} \\
k_a &= 0.1\ \text{s}^{-1} \\
k_d &= 0.001\ \text{s}^{-1} \\
k_{\text{wee1,basal}} &= 0.005\ \text{s}^{-1} \\
k_{\text{cdc25,basal}} &= 0.01\ \text{s}^{-1} \\
k_{\text{wee1}} &= 0.05\ \text{s}^{-1} \\
k_{\text{cdc25}} &= 0.1\ \text{s}^{-1} \\
[\text{cyclin}]_{\text{tot}} &= 230\ \text{nM} \\
[\text{Cdc25}]_{\text{tot}} &= 15\ \text{nM} \\
[\text{Wee1}]_{\text{tot}} &= 15\ \text{nM} \\
[\text{APC}]_{\text{tot}} &= 50\ \text{nM} \\
[\text{Plx}]_{\text{tot}} &= 50\ \text{nM} \\
n_{\text{wee1}} &= 4 \\
n_{\text{cdc25}} &= 4 \\
n_{\text{APC}} &= 4 \\
n_{\text{plx1}} &= 4 \\
\text{EC50}_{\text{plx1}} &= 40\ \text{nM} \\
\text{EC50}_{\text{wee1}} &= 40\ \text{nM} \\
\text{EC50}_{\text{cdc25}} &= 40\ \text{nM} \\
\text{EC50}_{\text{APC}} &= 40\ \text{nM} \\
k_{\text{cdc25,on}} &= 1.75\ \text{s}^{-1} \\
k_{\text{cdc25,off}} &= 0.2\ \text{s}^{-1} \\
k_{\text{APC,on}} &= 1\ \text{s}^{-1} \\
k_{\text{APC,off}} &= 0.15\ \text{s}^{-1} \\
k_{\text{plx1,on}} &= 1\ \text{s}^{-1} \\
k_{\text{plx1,off}} &= 0.15\ \text{s}^{-1} \\
k_{\text{wee1,on}} &= 0.2\ \text{s}^{-1} \\
k_{\text{wee1,off}} &= 1.75\ \text{s}^{-1} \\
k_{\text{cak}} &= 0.8\ \text{s}^{-1} \\
k_{\text{pp2c}} &= 0.008\ \text{s}^{-1}
\end{aligned}$$

2.2. Cell cycle model 2

This cell cycle model was introduced in Ref. (Yang and Ferrell, 2013) and consists of 2 ODEs. The first ODE describes the activity of Cdk1 in its active phosphorylation state (in cell cycle model 1, the equivalent species is cyclin B-Cdk1-Tp), while the second equation describes the synthesis and destruction of the mitotic cyclins:

$$\begin{aligned}\frac{d[\text{Cdk1}]}{dt} &= k_s + k_{\text{cdc25}} Cdc25^*([\text{Cdk1}])\,([\text{cyclin B}] - [\text{Cdk1}]) \\ &\quad -k_{\text{wee1}} Wee1^*([\text{Cdk1}])[\text{Cdk1}] - k_d([\text{Cdk1}])[\text{Cdk1}], \end{aligned} \tag{10}$$

$$\frac{d[\text{cyclin B}]}{dt} = k_s - k_d\,([\text{Cdk1}])\,[\text{cyclin B}], \tag{11}$$

where $k_d([\text{Cdk1}])$, $Cdc25^*([\text{Cdk1}])$ and $Wee1^*([\text{Cdk1}])$ are all ultrasensitive functions of Cdk1:

$$k_d([\text{Cdk1}]) = a_d + b_d \frac{[\text{Cdk1}]^{n_d}}{[\text{Cdk1}]^{n_d} + \text{EC50}_d^{n_d}}, \tag{12}$$

$$k_{\text{cdc25}} Cdc25^*([\text{Cdk1}]) = a_{\text{cdc25}} + b_{\text{cdc25}} \frac{[\text{Cdk1}]^{n_c}}{[\text{Cdk1}]^{n_c} + \text{EC50}_d^{n_c}}, \tag{13}$$

$$k_{\text{wee1}} Wee1^*([\text{Cdk1}]) = a_{\text{wee1}} + b_{\text{wee1}} \frac{\text{EC50}_d^{n_w}}{[\text{Cdk1}]^{n_w} + \text{EC50}_d^{n_w}}. \tag{14}$$

Unless mentioned otherwise, the parameters used were:

$$\begin{aligned} k_s &= 1.5/60\ \text{s}^{-1} \\ a_d &= 0.01/60\ \text{s}^{-1} \\ b_d &= 0.06/60\ \text{s}^{-1} \\ \text{EC50}_d &= 32\ \text{nM} \\ n_d &= 17 \\ a_{\text{cdc25}} &= 0.8/60\ \text{s}^{-1} \\ b_{\text{cdc25}} &= 4/60\ \text{s}^{-1} \\ \text{EC50}_c &= 35\ \text{nM} \\ n_c &= 11 \\ a_w &= 0.4/60\ \text{s}^{-1} \\ b_w &= 2/60\ \text{s}^{-1} \\ \text{EC50}_w &= 30\ \text{nM} \\ n_w &= 3.5 \end{aligned}$$

2.3. Asymmetric FitzHugh-Nagumo model

The generic FitzHugh-Nagumo (FHN) equations (Fitzhugh, 1961; Nagumo J., 1964) allow for the simple generation of bistability, excitability, and relaxation oscillations (Gelens et al., 2014). In our simulations, the parameters were chosen such that the FHN model admits relaxation oscillations in its variables u and v, where u represents cyclin B-Cdk1 activity and v represents the more slowly varying cyclin B concentration. The equations are as follows:

$$\frac{du}{dt} = u - u^3 - v, \tag{15}$$

$$\frac{dv}{dt} = \varepsilon(u)[u - bv - a]. \tag{16}$$

In order to be able to tune the pulse duration of the oscillations, we introduced the function $\varepsilon(u)$:

$$\varepsilon(u) = \varepsilon + \gamma(1-\varepsilon)\frac{\text{sign}(u)+1}{2}, \tag{17}$$

such that for $\gamma = 0$, $\varepsilon(u) = \varepsilon$, and for $\gamma = 1$, $\varepsilon(u) = 1$, allowing us to tune the slow time scale by varying ε between its minimal value at $\gamma = 0$ and its maximal value of 1. Throughout, we use $a = 0$, $b = 0.5$, and $\varepsilon = 10^{-3}$ (unless mentioned otherwise); with these parameters, we observed oscillations with long pulse duration for $\gamma = 0.01$ and short pulse duration for $\gamma = 1$. All concentrations, times, and rates are in normalized form and are thus in arbitrary units (a.u.).

2.4. Spatial diffusive coupling

Following Refs. (McIsaac et al., 2011;Chang and Ferrell, 2013), we introduced spatial diffusion of all cell-cycle proteins. As most of these proteins have similar molecular weights (see (McIsaac et al., 2011)), for cell cycle models 1 and 2, we assumed a constant diffusion constant $D = 10\ \mu\text{m}^2/s$ for all proteins. For the asymmetric FHN model, we set $D = 1$. For each protein concentration $c(x,t)$, we added a diffusion term to each ODE as follows:

$$\frac{dc(x,t)}{dt} = \cdots + D\frac{\partial^2 c(x,t)}{\partial x^2}.$$

3. Numerical methods and initialization of simulations

We implemented a numerical integration scheme in C for our reaction-diffusion models using periodic boundary conditions, allowing use of fast Fourier transforms. A two-step method was implemented that is pseudo-spectral and accurate up to second order in time. We also verified our results using a Crank-Nicolson method. Here, we describe the relevant numerical and initialization details for each of the figures.

3.1. Figure 1: Setup of numerical simulations

We simulated the time series of Cdk1 activity using cell cycle model 1 for two calcium wave speeds: (A) $vel = 50$ μm/s and (B) $vel = 10$ μm/s (C). $N = 512$ discretization points were used, and the domain width was $L = 2000$ μm. Only half of the domain is shown in Figure 1. The discretization time step was $\delta t = 0.01$. All protein concentrations were initialized to zero and then evolved over 2500 s in the absence of any APC activity ($d[\mathrm{APC}]_{\mathrm{act}}/dt = 0$), such that the system finds itself in M-phase in the entire space. Next, APC activity was gradually turned on, with the timing defined by the passage of a wave past a certain location. This wave started at $t = 2500$ s in the center of the space ($x = 0$) and then spread out symmetrically with speed vel to the boundaries at $x = -1000$ μm and $x = 1000$ μm. The spatiotemporal correlation function for a protein $c(x, t)$ was calculated as

$$\mathrm{Corr}(\delta x, \delta t) = \langle \delta c(x, t) \delta c(x', t') \rangle,$$

where $\delta c \equiv c(x, t) - \langle c(x, t) \rangle$ and $\langle c(x, t) \rangle$ is the average value of $c(x, t)$ over time and space, and $\delta x = x - x'$ and $\delta t = t - t'$. The correlation function was calculated using the last 1 h of the simulation and using half of the spatial domain.

3.2. Figure 3: Setup of numerical simulations

We simulated the time series of Cdk1 activity using cell cycle model 1, cell cycle model 2, and the FHN model for two wave speeds that define the start of APC activity, which coincides with the exit from M-phase (or the upper state in the case of the FHN model). $N = 512$ discretization points were used, with a domain size of $L = 2000$. Only half of the domain is shown. The parameters were chosen to be homogeneous throughout space, and a heterogeneity in initiation time was introduced by having the cell cycle initiated by a calcium wave of velocity vel spreading through the system. Below we provide details of the numerics specific to each model.

- Cell cycle model 1 (D,G): The discretization time step was $\delta t = 0.01$ and Cdk1 activity was recorded and plotted every 10 s. The total simulation time was 300 min after initiation of the activation wave. The activation speed was $vel = 10$ μm/s. For the top panels in (D,G), $k_{\mathrm{dest}} = 0.0001$, while for the bottom panels $k_{\mathrm{dest}} = 0.01$. In (D), $D = 0$ and no activation wave was introduced, such that the whole space oscillated synchronously. In (G), $D = 10$ $\mu\mathrm{m}^2$/s and APC activity was started by the passing of a wave with speed vel that was initiated at $t = 0$ s.
- Cell cycle model 2 (E,H): The discretization time step was $\delta t = 0.01$ and Cdk1 activity was recorded and plotted every 12 s. The total simulation time was 300 min after initiation of the activation wave. The activation speed was $vel = 10$ μm/min. For the top panels in (E,H), $b_d = 0.06$, while for the bottom panels $b_d = 0.6$. In (E), $D = 0$ and no activation wave was introduced, such that the whole space oscillated synchronously. In (H), $D = 10$ $\mu\mathrm{m}^2$/s and APC activity was started by the passing of a wave with speed vel that was initiated at $t = 0$ s.
- FHN model (F,I): The discretization time step was $\delta t = 0.01$ and the value of u was recorded and plotted every 10 time units. The total simulation time was 10000. The activation speed was $vel = 1$. For the top panels in (F,I), $\gamma = 0.01$, while for the bottom panels $\gamma = 1$. In (F), $D = 0$ and no activation wave was introduced, such that the whole region in space oscillated synchronously. In (I), $D = 1$ and degradation of u with u in the upper state was started by the passing of a wave with speed vel that was initiated at $t = 0$.

3.3. Figure 4: Setup of numerical simulations

We simulated the spatiotemporal evolution of u using the FHN model under two conditions: (A,C) $\gamma = 1$ and (B,D) $\gamma = 0.01$. In both cases, $D = 1$. $N = 512$ spatial discretization points were used, and the domain width was $L = 2000$. The discretization time step was $\delta t = 0.01$ and the value of u was recorded every 0.1 time units. This sampling rate was verified to provide sufficiently dense sampling, even during the sharpest variations of u

(such as in (A)). Total simulation time was 100000 and the trajectories in Figure 4 were plotted using the last 85000 time units, allowing the system to relax to its stable attractor for 15000 time units (which was verified to be sufficient). (C,D) include the nullclines for u and v defined by:

$$\begin{aligned} 0 &= u - u^3 - v, \\ 0 &= \varepsilon(u)[u - bv - a]. \end{aligned}$$

3.4. Figure 5: Setup of numerical simulations

In Figure 5, using the FHN model, we show that chaotic dynamics can be triggered by spatial heterogeneities, either in the initial conditions (A) or in the biochemical parameters (B,C). The simulations were carried out with a time step $\delta t = 0.01$, $N = 512$ discretization points, and a domain size of $L = 2000$. In (A,D,G), the initial conditions varied in space, because the time at which APC becomes active in the dynamics, triggering mitotic exit at a certain location, depends on the speed of the calcium wave. All parameters were homogeneous in space ($b = 0.5, a = 0, \varepsilon = 10^{-3}$). In (B,E,H), the same biochemical parameters were used, but the initial conditions were homogeneous in space and APC was active from the start. Instead, the value of ε was increased in a central region of width 43 grid points from 10^{-3} to $10^{-2.9}$. In (C,F,I), the initial conditions were also spatially homogeneous, and the value of ε varied randomly over space. ε was chosen such that $-\log_{10}(\varepsilon) = \rho$, where ρ was randomly chosen at each discretization point from a Gaussian distribution with mean 3 and standard deviation 0.1. In (D-F), the value of γ was 0.01, while in (G-I), $\gamma = 1$.

3.5. Figure 6: Setup of numerical simulations

In Figure 6, using the FHN model, we show that there is a trade-off between the pulse duration of the reaction and the diffusion strength in the generation of chaos (or more generally: the generation of defects). The simulations have been carried out with a time step $\delta t = 0.01$, and a spatial discretization size of 0.3. The setup of the simulations was similar to Figure 5B. A central pacemaker region of width 40 was defined in which $b = 0.5$, while in the remainder of the domain $b = 1$. $a = 0$ and $\varepsilon = 10^{-3}$ throughout the domain. In (A-C), the domain size $L = 500$ and $\gamma = 0.5$, while the diffusion strength was varied ($D = 30$ (A), 10 (B), 1 (C)). By varying the diffusion strength $\log_{10} D$ in steps of 0.05, we determined the critical value of D at which the trigger waves were no longer able to dominate the whole domain and defects formed. This critical value of D was calculated for different values of γ and provided the boundary presented in (D). In (E), we show how the pulse duty cycle changes with γ, where we define the duty cycle as the area under the curve during a pulse (when $u > 0$) vs. the area under the curve when $u < 0$. The duty cycle scales linearly with γ on a log-log scale up to $\gamma \approx 0.2$, after which the curve deviates from the linear fit (red line). Next, we numerically evaluated the system dynamics for varying domain sizes ($L = 500$ (F), 100 (G), 50 (H)) for fixed values of $D = 1$ and $\gamma = 1$. Similar to (D), we repeated the numerical calculation of the critical values of D for these three different domain sizes (I). Finally, keeping $\gamma = 1$, we plot the dependence of this critical diffusion strength as a function of the domain size L.

4. Supplemental Movies

4.1. Movie S1, Related to Figure 2.

Rapid fertilization waves in embryos fertilized at 23°C. The movie lasts for 20 min and the frame rate used was 1 frame every 10 s.

4.2. Movie S2, Related to Figure 2.

Slower fertilization waves in embryos fertilized at 13°C. The movie lasts for 20 min and the frame rate used was 1 frame every 10 s.

4.3. Movie S3, Related to Figure 2.

Normal development in embryos fertilized at either 13°C or 23°C and then allowed to develop at 23°C. One batch of eggs was fertilized at 13°C and then returned to 23°C after the calcium wave had passed (20 min after fertilization). A second batch of eggs from the same frog was fertilized at 23°C at the same time and always maintained at 23°C. The movie starts 28 min after fertilization and continues up to approximately 33 h after fertilization. One frame was taken every 30 s. The second part of the movie is played 5 times faster as indicated.

5. Supplemental References

Chang, J.B., and Ferrell, J.E., Jr. (2013). Mitotic trigger waves and the spatial coordination of the Xenopus cell cycle. Nature 500, 603-607.

Fitzhugh, R. (1961). Impulses and physiological states in theoretical models of nerve membrane. Biophysical journal 1, 445-466.

Gelens, L., Anderson, G.A., and Ferrell, J.E., Jr. (2014). Spatial trigger waves: positive feedback gets you a long way. Molecular biology of the cell 25, 3486-3493.

McIsaac, R.S., Huang, K.C., Sengupta, A., and Wingreen, N.S. (2011). Does the potential for chaos constrain the embryonic cell-cycle oscillator? PLoS computational biology 7, e1002109.

Nagumo J., A.S., Yoshizawa S. (1964). An active pulse transmission line simulating nerve axon. Proc IRE 50, 2061-2070.

Pomerening, J.R., Kim, S.Y., and Ferrell, J.E., Jr. (2005). Systems-level dissection of the cell-cycle oscillator: bypassing positive feedback produces damped oscillations. Cell 122, 565-578.

Pomerening, J.R., Sontag, E.D., and Ferrell, J.E., Jr. (2003). Building a cell cycle oscillator: hysteresis and bistability in the activation of Cdc2. Nature cell biology 5, 346-351.

Yang, Q., and Ferrell, J.E., Jr. (2013). The Cdk1-APC/C cell cycle oscillator circuit functions as a time-delayed, ultrasensitive switch. Nature cell biology 15, 519-525.